Computational and Structural Biotechnology Journal 23 (2024) 2418–2428

Contents lists available at ScienceDirect

Computational and Structural Biotechnology Journal

journal homepage: www.elsevier.com/locate/csbj

Research Article

Isomer-sourced structure iteration methods for *in silico* development of inhibitors: Inducing GTP-bound NRAS-Q61 oncogenic mutations to an "off-like" state

Zheyao Hu, Jordi Martí *

Department of Physics, Polytechnic University of Catalonia-Barcelona Tech, B4-B5 Northern Campus UPC, Barcelona, 08034, Catalonia, Spain

ARTICLE INFO

Keywords:
Molecular mechanisms
Drug design
NRAS oncogenes
ISSI method
HM-387 compound

ABSTRACT

The NRAS-mutant subset of melanoma represent some of the most aggressive and deadliest types associated with poor overall survival. Unfortunately, for more than 40 years, no therapeutic agent directly targeting NRAS mutations has been clinically approved. In this work, based on microsecond scale molecular dynamics simulations, the effect of Q61 mutations on NRAS conformational characteristics is revealed at the atomic level. The GTP-bound NRAS-Q61R and Q61K mutations show a specific targetable pocket between Switch-II and α-helix 3 whereas the NRAS-Q61L non-polar mutation category shows a different targetable pocket. Moreover, a new isomer-sourced structure iteration method has been developed for the *in silico* design of potential inhibitor prototypes for oncogenes. We show the possibility of a designed prototype HM-387 to target activated NRAS-Q61R and that it can gradually induce the transition from the activated NRAS-Q61R to an "off-like" state.

1. Introduction

The RAS family is the most frequently mutated oncogene in some cancers, such as melanoma, lung and pancreatic cancer [1,2]. Clinical data indicate that the most frequently mutated RAS isoforms vary by tissue and cancer types [3]. In particular, neuroblastoma RAS viral (v-ras) oncogene homolog (NRAS) is the most frequently mutated RAS isoform in melanoma, with the mutated codon typically occurring at residue 61 [2,3]. Together with keratinocyte carcinoma [4], melanoma is one of the most common cutaneous cancers worldwide and the one annually causing the largest number of deaths [5]. The NRAS-mutant subset of melanoma shows aggressive clinical behaviour and a poor prognosis, and it is associated with low overall survival [6,7]. Among a variety of immunotherapies available to patients with cancers related to NRAS oncogenes [7], there is still a lack of efficient strategies capable of directly targeting NRAS [8–10]. For instance, some strategies such as the use of MEK inhibitors are quite promising, but still with low clinical efficiency [11]. In 2018, the US Food and Drug Administration approved preliminary treatments based on drugs encorafenib and binimetinib [12], but no significant success was observed. Therefore, the detailed conformation and local structure of NRAS is necessary to reveal potential targeting pockets that may facilitate the discovery of potential drug-like compounds.

Drug discovery is an extremely expensive, lengthy and interdisciplinary subject. A new approved drug usually costs several billion dollars and takes decades to develop [13]. *In silico* drug design can be involved in many stages of drug development, especially in the discovery of initial compounds of promising potential applicability [14]. Nowadays, with the development of computational resources and methods [15–19] together with the proliferation of experimental protein structural data [20], the use of computational physics and molecular modelling [21,22] for computer-aided drug design has gained enormous momentum. In this way, several *in silico* drug design methods have been recently released [23–26]. Differently to other authors who used combined tools for drug design or screening such as Gou et al. [27], Sadybekov et al. [28] or Xu et al. [29], our aim in this paper is to provide a new simple but efficient computational protocol able to improve the efficiency in the design of new potentially useful chemical templates, avoiding the large-scale screening among hundreds of compounds.

In this work, benefiting from the fact that molecular dynamics (MD) simulations use accurate force fields and can capture the detailed be-

* Corresponding author.
E-mail address: jordi.marti@upc.edu (J. Martí).

https://doi.org/10.1016/j.csbj.2024.05.038
Received 25 March 2024; Received in revised form 20 May 2024; Accepted 21 May 2024
Available online 24 May 2024

haviour and interactions of biomolecules at the all-atom level with excellent temporal resolution, the impact of NRAS-Q61 mutations on its structural conformation has been investigated. According to the detailed analysis of the MD trajectories harvested at the microsecond time scale, we distinguish different characteristics of conformational changes between NRAS-Q61 mutations and also reveal the detailed molecular interactions responsible for the behaviour of mutated NRAS at the all-atom level. Subsequently, a targetable pocket on GTP-bound NRAS Q61 positively charged mutants (Q61R and Q61K) is revealed. Further, taking GTP-bound NRAS-Q61R as example and combining structural iteration, virtual screening and MD simulations, we introduce a new *isomer-sourced structure iteration method* (ISSI) for the development of potentially effective compounds. In this regard, we are reporting, as an example of the use of ISSI, a prototype compound (designed as HM-387) which might be able to target positively charged NRAS-Q61 mutations. We expect to provide valuable information that can foster subsequent medicinal development in wet lab experiments.

2. Results and discussion

In this section, we have investigated the microscopic structure of the eight main GTP-bound/GDP-bound NRAS isoforms in aqueous ionic solution. The difference between the mutated NRAS species is located at codon 61, with the sequences of the eight isoforms shown in Fig. 1 of "Supplementary Material" (SM). As general procedures, we have adopted microsecond-scale MD simulations as the main computational tool [30], assuming the successful CHARMM36m force field [31] to model all simulated systems. All simulations were performed by means of the GROMACS/2021 package released on January 28th, 2021 [32] and crystal structures of GDP/GTP NRAS proteins were obtained from RCSB PDB Protein Data Bank [33]. All of our results have been averaged from three independent MD trajectories for each NRAS isoform. Radial distribution functions and potentials of mean force have been employed to reveal the atomic-level interactions corresponding to the conformational changes of the different NRAS-Q61 mutants. Finally, in this paper we introduce a new protocol able to develop potential compounds *in silico* and we apply it to the case of NRAS-Q61R mutations. Atomic detail sketches of the main residues for each compound and all procedures, data and figures related to the ISSI method are reported in SM for the sake of clarity of the manuscript.

2.1. Structural characteristics of NRAS isoforms and the effect of Q61 mutations on their conformational changes

Firstly, we computed Root Mean Square Deviations (RMSD, Fig. 1 A-D) and Root Mean Square Fluctuations (RMSF, Fig. 1 E-H) in order to investigate the overall conformational fluctuations and stability of NRAS-WT (wild type) and the three mutant isoforms considered in the present work, i.e. NRAS-Q61R, NRAS-Q61K and NRAS-Q61L (Fig. 1). On the one hand, RMSD is defined by Eq. (1):

$$RMSD(t) \equiv \sqrt{\frac{1}{N}\sum_{i=1}^{N}\delta_i^2(t)}, \tag{1}$$

where δ_i is the difference in distance between the atom i (located at $x_i(t)$) of the catalytic domain and the equivalent location in the crystal structure whereas, on the other hand, RMSF are defined by Eq. (2):

$$RMSF_i \equiv \sqrt{\frac{1}{\Delta t}\sum_{t_j=1}^{\Delta t}(x_i(t_j)-\tilde{x}_i)^2}, \tag{2}$$

where $\tilde{x}_i$ is the time average of x_i and Δt is the time interval where the average has been taken. The equilibration part of the MD trajectories corresponds to the initial 1 μs in all RMSD plots.

From the results of Fig. 1, we can observe that the overall conformational fluctuations of the GTP-bound NRAS are lower than those of the GDP-bound NRAS in all cases. Comparing to KRAS species, which show distinct conformations [34], NRAS species keep their conformational fluctuations in a relatively small range. The RMSD of GTP-bound NRAS-WT fluctuates stably around 0.25 nm with several short fluctuations (between ~0.3 and 0.4 nm). When GTP is hydrolysed to GDP, the average value and range of the fluctuations of NRAS-WT increase significantly. GTP-bound NRAS displays significant conformational stability when Q61 is mutated to R61 (RMSD ~0.12 nm) but when GTP is converted to GDP, the conformational fluctuations of NRAS-Q61R returns to a similar extent as that of GDP-bound NRAS-WT. Further, the RMSD characteristics of other mutations (Q61K and Q61L) are similar to those of GTP/GDP-bound NRAS-WT. In addition we should notice that error bars at each point, computed as the largest deviation of all three trajectories compared to the average, reveal in some cases (NRAS-WT-GDP, for instance) significant fluctuations of RMSD and/or RMSF, but no alteration of the main trends of each property has been observed in any case.

The ensuing RMSF indicate that the conformational dynamics of NRAS-WT and its mutants are mainly reflected by structural changes of Switch-I (SW-I, residues 27-37) and Switch-II (SW-II, residues 58-64). This is fully consistent with previously reported findings [34–37]. In the GTP-bound NRAS-WT case the flexibility of the SW-I is around 1.2 fold larger than that of SW-II. When GTP is hydrolysed into GDP, the flexibility of SW-I/II increases simultaneously by about 1.5 fold, in a consistent way with the RMSD trend of NRAS-WT. When Q61 is mutated, the overall flexibility of SW-I/II of the GTP-bound NRAS mutants is similar to that of NRAS-WT, with the exception of SW-I in GTP-bound NRAS-Q61R, with significantly reduced fluctuations. Noticeably, in the case of GDP-bound NRAS mutants, similar characteristics were exhibited among the positively charged mutants of Q61 (Q61R and Q61K), namely the flexibility of SW-I decreased slightly compared to the WT case, whereas the RMSF values of SW-II increased leading to similar flexibilities of SW-I and SW-II. Interestingly, the RMSF trend of the non-polar mutation (GDP-bound NRAS-Q61L) was opposite to that of positively charged mutations: The flexibility of the SW-II region is significantly suppressed (~1 fold) compared with the NRAS-WT and NRAS-Q61 positively charged mutations.

The RMSD and RMSF data in Fig. 1 show the overall conformational fluctuations of NRAS and the corresponding active domains (mainly SW-I and SW-II). We further performed the so-called "Residue Cross Correlation" analysis [38,39] in order to investigate the correlation of residue-to-residue motion within NRAS. Results are displayed in Fig. 2. Snapshots of representative configurations corresponding to each case have been included as a help for the visualisation of the results.

For NRAS-WT (Fig. 2 A and B), the residue cross correlations of GTP-bound NRAS-WT and GDP-bound NRAS-WT are similar. SW-I exhibits the trend of separating from SW-II and from the main structure of the NRAS-WT, whereas SW-II behaves differently: it shows a tendency to be closer to P-loop (residues 10-14) and α-helix 3 (residues 86-105). The mutations of NRAS to positively charged side chains (Q61R and Q61K), show some significant differences to NRAS-WT. For GDP-bound NRAS-Q61R (Fig. 2 C), we can clearly observe that the behaviour of SW-II is opposite to that of NRAS-WT: SW-II tends to separate from the main body of NRAS-Q61R in a drastic fashion (e.g. the P-loop and α-helix 3). Besides, both SW-I/II tend to be close each other and their surfaces in close contact (Fig. 2 C right side). The residue cross correlations of GTP-bound NRAS-Q61R are similar to GDP-bound NRAS-Q61R, but the conformational stability of GTP-bound NRAS-Q61R is significantly greater than that of GDP-bound NRAS-Q61R. Another difference from GDP-bound NRAS-Q61R is that SW-II can contact the P-loop and it is slightly separated from the surface of α-helix 3, forming a smaller cavity. Interestingly, both of the generated cavities on the surfaces of GDP-bound NRAS-Q61R (large) and GTP-bound NRAS-Q61R (small) may serve as targetable pockets. The residue cross correlation results of NRAS-Q61K (Fig. 2 E and F) show features very similar to those of

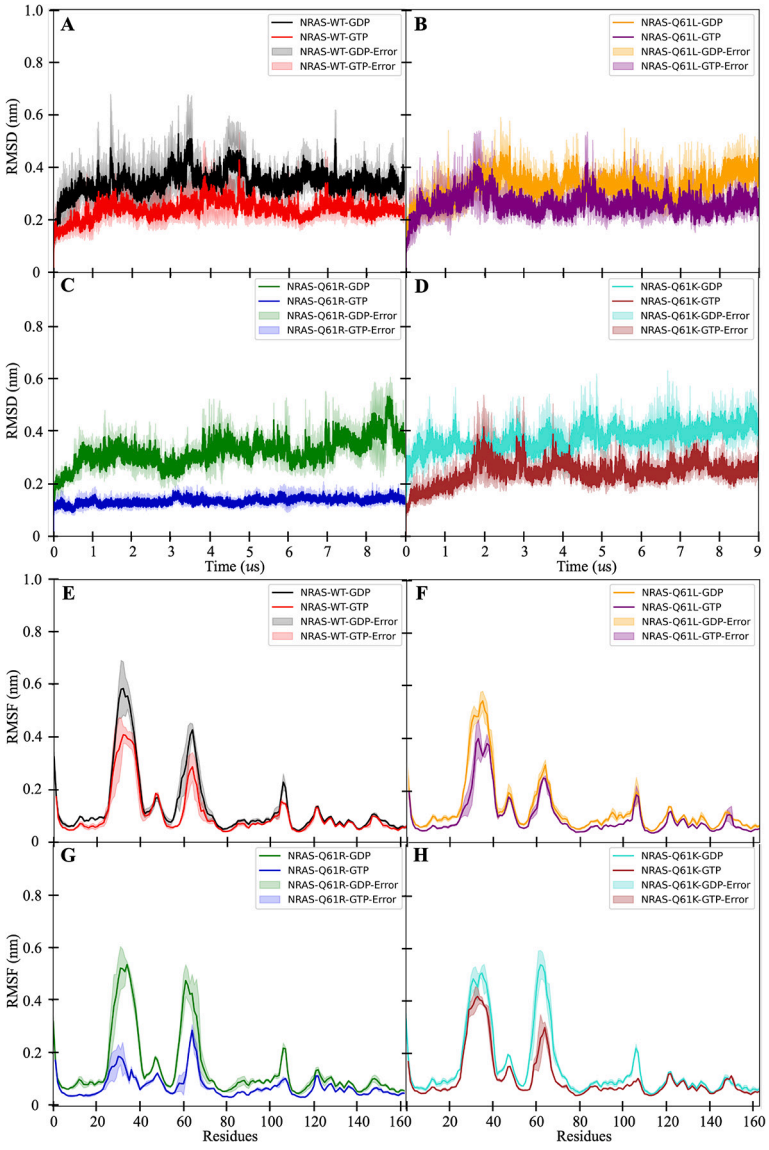

Fig. 1. The impact of Q61 mutations on the dynamic properties of NRAS, from the perspective of RMSD and RMSF. (A)-(D) RMSD of NRAS wild type and its Q61 mutant isoforms with the corresponding error bars; (E)-(H) RMSF of NRAS wild type and its Q61 mutant isoforms with the corresponding error bars. The RMSD/RMSF are averaged from 3 independent trajectories, and in all cases only "backbone" atoms of NRAS were considered.

NRAS-Q61R, with GDP-bound NRAS-Q61K holding a large targetable pocket and GTP-bound NRAS-Q61K holding a small one. When Q61 is mutated to the non-polar amino acid LEU (case NRAS-Q61L, Fig. 2 G and H), the dynamical trends of SW-I/II maintain a similar fashion to those in NRAS-WT, whereas SW-II shows a stronger tendency to be closer to the P-loop and α-helix 3 regions than NRAS-WT.

We can conclude that positively charged mutations Q61R and Q61K (henceforth named as R61 and K61, respectively) provide conformations topologically very different of wild type (renamed Q61) and the non-polar mutation Q61L (renamed as L61). The data collected suggest three general features: (1) to a large extent, NRAS are similar to other RAS family proteins, with their conformational changes mainly embodied by SW-I and SW-II [40,41,34]; (2) the Q61 mutations of NRAS have high impact on NRAS conformational changes [42,43,3]; (3) there may exist different specific interactions able to drive meaningful conformational changes of different NRAS isoforms, as they will be described below in Section 2.2.

2.2. The different atomic-level interactions driving conformational changes of NRAS

The previous study shows that different types of Q61 mutations can have different effects on the conformational changes of NRAS. Hence, according to Section 2.1 positively charged R61 and K61 mutations can be grouped into the same class and the non-polar mutation L61 should be grouped into a different class. In this Section, we will analyse the characteristics of the two distinct mutant groups described above, especially regarding their interactions with solvating water molecules. We start considering the so-called atomic pair radial distribution functions $g_{AB}(r)$ (RDF, defined in Eq. (3)) to explore the changes in the ability of NRAS to form hydrogen bonds (HB) with water molecules, as reported in Fig. 3(A-H).

$$g_{AB}(r) = \frac{V \langle n_B(r) \rangle}{4\, N_B\, \pi r^2\, \Delta r}, \tag{3}$$

where $n_B(r)$ is the number of atoms of species B surrounding a given atom of species A inside a spherical shell of width Δr. V is the total volume of the system and N_B is the total number of particles of species B.

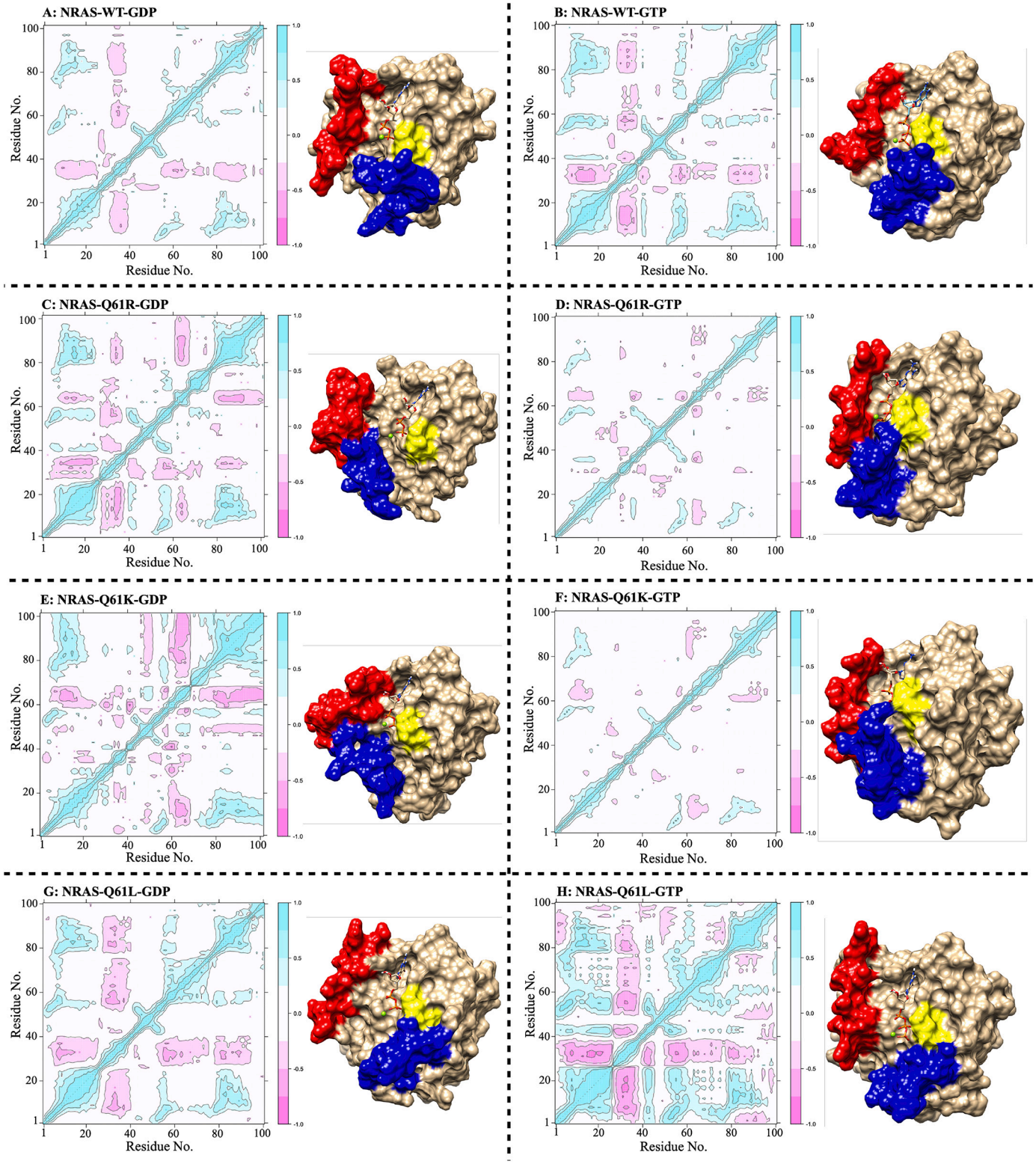

Fig. 2. The "Residue Cross Correlation" analysis of the NRAS wild type and its Q61 mutant isoforms. Highly (anti)correlated motions are depicted in cyan(pink). The figures at the right side of the residual cross correlation plots are the surface version of representative GTP/GDP-bound NRAS, yellow: P-loop, red: SW-I and blue: SW-II.

As a general feature, the active sites of the NRAS-Q61 side chain capable of forming HB are oxygen "O1", hydrogen "H1" and hydrogen "H2" (Fig. 3 A and E, defined in Fig. 2 of SM). In both GTP/GDP-bound NRAS-WT case, "O1" can form HB with water with a length of around 1.85 Å, typical of bonds formed by biomolecules and water [44,45]. The ability of "H1" and "H2" to form HB with solvating water is lower than that of "O1", given the shorter height of the RDF, showing a HB length of 2.05 Å. The active sites of R61 side chain capable of forming HB are "H1" to "H5" (Fig. 3 B and F, defined in Fig. 2 in SM). The GTP-bound NRAS-R61 shows a characteristic HB length of 1.85 Å, with the first maximum of RDF smaller than that of "O1" but higher than those of "H1" and "H2" from the NRAS-WT case (Fig. 3 E). When GTP is hydrol-

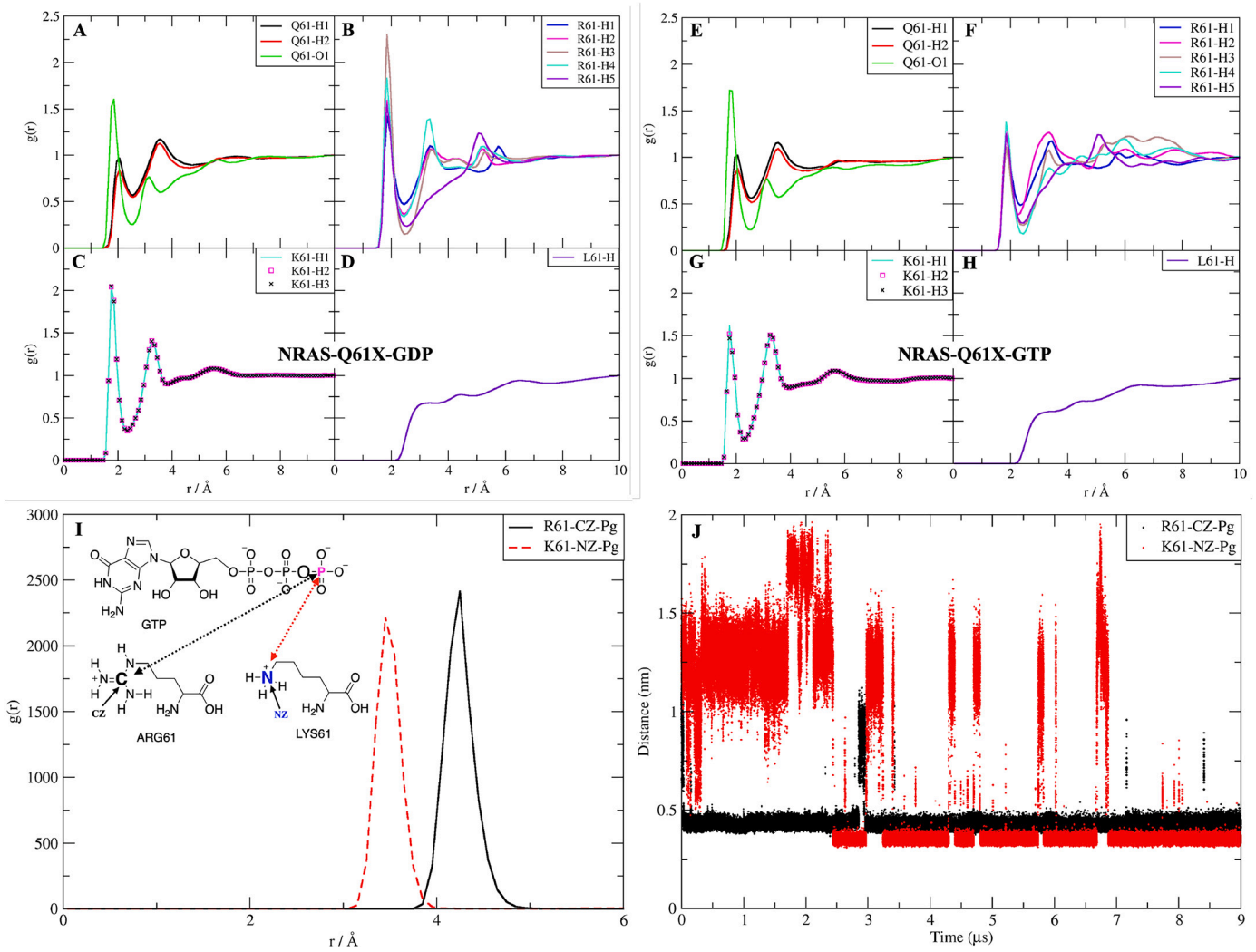

Fig. 3. Radial distribution function analysis of the 61 st. amino acid of GDP/GTP-bound NRAS with water. (A) NRAS-WT-GDP; (B) NRAS-R61-GDP; (C) NRAS-K61-GDP; (D) NRAS-L61-GDP; (E) NRAS-WT-GTP; (F) NRAS-R61-GTP; (G) NRAS-K61-GTP; (H) NRAS-L61-GTP; (I) RDF value of R61/K61 interaction with terminal Pγ, with structures of GTP, R61 (residue ARG), K61 (residue LYS) and distances taken to calculate the corresponding RDF; (J) Time-dependent atomic distances between R61-CZ/K61-NZ and Pγ.

ysed to GDP, the interactions between active hydrogens and water are greatly enhanced (Fig. 3 B). For the R61 case, we can conclude that: (1) R61 has more active hydrogens and the interaction of R61 with water is enhanced; (2) the phosphate tail of GTP (represented by the terminal phosphorus Pγ located at the end of the GTP tail) can form strong HB interactions with R61 (sketch in Fig. 3 I and distance distributions shown in sub-plot J), allowing NRAS-R61 to maintain relatively low conformational fluctuations and to exist a small targetable cave between SW-II and α-helix 3 (see Fig. 2 D). However, since the phosphate tail of GDP is shortened, the HB interaction between R61 and the phosphate tail vanishes. Finally, in this latter case the SW-II is stripped from the protein surface under the interaction of aqueous solution and forming a large targetable pocket (Fig. 2 C).

The main features of the RDF of NRAS-K61 hold similar trends as those of NRAS-R61. Three active hydrogens (defined in Fig. 2 of SM) forming HBs with water or GTP (Fig. 3 C, G, I and J). The RDF of a single hydrogen atom in GTP-bound NRAS-K61 (Fig. 3 G) is slightly increased compared to GTP-bound NRAS-R61. This is because the side chain of K61 is shorter than that of R61 and the HB effect between K61 and GTP phosphate is weakened. Interestingly, the RDF of the three hydrogens almost coincide with the GDP-bound NRAS-K61 case (Fig. 3 C). This is due to the fact that K61 is completely dissolved by the aqueous solution and the three hydrogens of amino group of K61 are equivalent to each other, so that water has the same probability of forming HB with them. This also aligns well with the concept of “equivalent hydrogen” in organic chemistry. Contrary to Q61, R61 and K61, the mutation L61 showed no HB at all (Fig. 3 D and H), indicating strong hydrophobic characteristics.

In order to further analyse the degree of the enhanced HB interaction with the aqueous solution when Q61 is mutated to positively charged amino acids, we consider the radial distances between two species as our order parameters to calculate the potential of mean force (PMF) through the so-called reversible work $W_{AB}(r)$ [46,47], as defined by Eq. (4):

$$W_{AB}(r) = -\frac{1}{\beta} \ln g_{AB}(r), \tag{4}$$

where $\beta = 1/(k_B T)$ is the Boltzmann factor, k_B the Boltzmann constant and T the temperature. This specific free-energy calculation has been considered only for the residue 61-water interactions, instead of the more complex interactions related to GTP/GDP and other NRAS residues. In general, when multidimensional reaction coordinates are involved, other methods such as metadynamics [48,49] of transition path sampling [50–52] should be used, but they are out of the scope of this work. A free-energy barrier defined by a neat first minimum and a first maximum of $W(r)$ (not shown) is clearly seen in all cases. The full

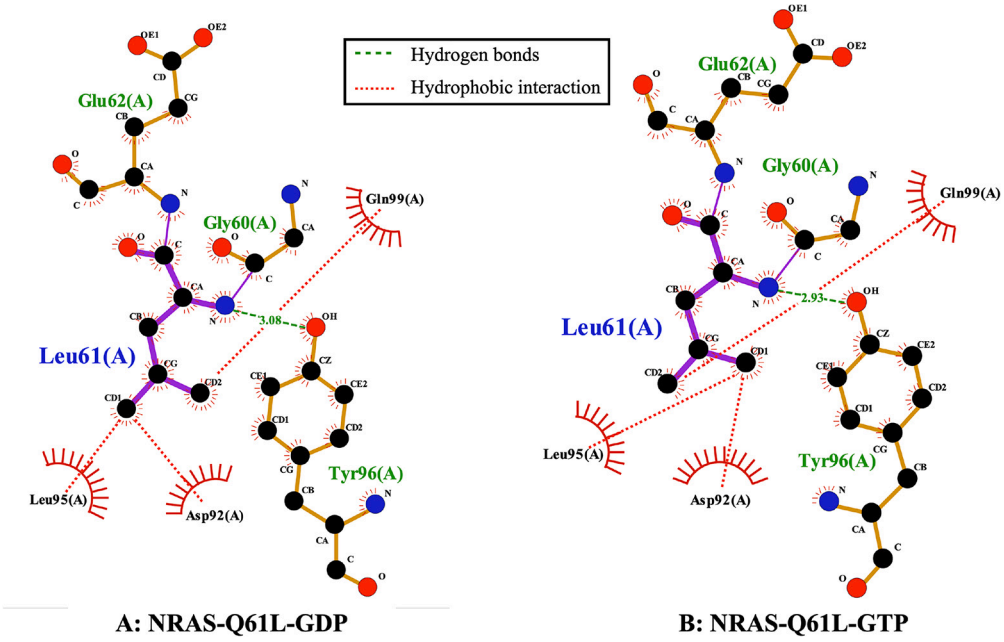

Fig. 4. The binding model of the detected hydrophobic pocket for NRAS-Q61L mutation. All distances in Å.

set of positions and free-energy barriers is reported in Table 1 and Table 2 of SM. We can observe overall barriers (adding up all contributions) of GDP-bound NRAS-Q61, R61 and K61 of 2.8, 8.9 and 5.4 k_BT, respectively (where 1 $k_BT = 0.616$ kcal/mol). This shows that when Q61 is mutated to the positively charged amino acids (R and K), the HB interaction of residue 61 with aqueous solution is enhanced by ∼ 2 to 3 fold, which may be one of the atomic-level forces driving the separation of SW-II from protein surfaces. Interestingly, for GTP bound NRAS, the overall barriers of Q61, R61 and K61 are of quite similar size (3.0, 6.9 and 4.9 k_BT, respectively). However, the strong HB interactions between GTP and R61/K61 keep SW-II bound to the protein surface, as it has been reported in Figs. 2 and 3.

For the non-polar L61 mutation, the characteristics of conformational changes are quite different from the positively charged mutations R61 and K61. A hydrophobic pocket on the α-helix 3 is detected (Fig. 4). This hydrophobic pocket is mainly composed of the hydrophobic structures (labelled in green in Fig. 2 of SM) of D92, L95, Y96 and Q99 side chains. During the dynamic evolution of L61, this hydrophobic pocket can capture the side chain of L61 and, simultaneously, the hydrogen "H1" of the amino group of the main chain of L61 can form a stable HB with the "O1" (also named "OH" in Fig. 4) of Y96, which further stabilises L61 and promotes the tight binding of SW-II to the α-helix 3. These sorts of specific interactions explain well the difference in conformational changes between L61 and other NRAS isoforms. In order to better characterise this special hydrophobic pocket of L61, we also displayed the time-dependent atomic group–group distances between selected amino acid residue side chains and the time-dependent atomic site–site distances between L61(H1) and Y96(O1), see Fig. 3 and Fig. 4 of SM.

From the fact that residue Q61 is also involved in the mechanism of GTP's hydrolysis by stabilising the transient hydronium ions around γ-phosphate, as it has been reported by several authors [53–57], we computed and compared the RDF of the three phosphorus of GTP (Pα, Pβ and Pγ) with water (oxygen atom), as it is reported in Fig. 5 of SM. The distribution of water around Pγ shows variations with the occurrence of Q61 mutations (Fig. 5C of SM). So, water can easily access to the Pγ phosphate of NRAS-WT, but when Q61 is mutated to R61 (K61), the distribution of water around the Pγ phosphate decreases sharply. This is consistent with the previous conclusions in Fig. 3. R61 and K61 can form HB with GTP, thus hindering the approach of water due to the steric hindrance effect. This also supports the fact that with the occurrence of mutations, the intrinsic GTPase ability will be reduced keeping the RAS molecular switch constitutively active [58–61]. Residue Q61L, due to the inability of L61 to form hydrogen bonds with GTP, tends to be anchored on the side of α-helix 3. Consequently, this positioning ensures that there is no significant reduction in the distribution of water molecules around Pγ due to the presence of the leucine side chain. However, when the residue 61L is anchored at the α-helix 3, the lack of stabilisation of transient hydronium ions around the γ-phosphate will also lead to the decrease in the potential rate of GTP's hydrolysis. Finally, for Pα and Pβ, both GTP/GDP bound NRAS-WT and their mutations reveal similar features. Moreover, when GTP hydrolyzes away (becoming GDP), the steric hindrance of Pβ decreases, making it easier for water to access Pβ.

2.3. *In silico development of potential inhibitors targeting NRAS-Q61 mutations using the ISSI method*

In the previous section, we investigated the conformational characteristics between wild-type NRAS and its Q61 mutants in detail. We found that when Q61 is mutated to positively charged amino acids (R and K), there exists a small targetable channel between SW-II and α-helix 3 on the surface of GTP-bound NRAS. Moreover there also exists a significant large targetable pocket on the surface of GDP-bound NRAS. We should consider that NRAS-R61 and K61 mutations are notorious for their strong GTP affinity and lack of intrinsic GTPase activity and, unlike the KRAS codon 12 mutants, these mutations are rarely found in the GDP-bound state. Hence, we have taken the targetable pocket on the surface of GTP-bound NRAS-R61 (depicted in Fig. 6 of SM) as a single target example to carry out corresponding *in silico* drug design, structure evolution and screening, aiming to provide a potential inhibitor template for potential further medicinal development. To do this, we introduce here a new procedure for *in silico* drug design, namely the isomer-sourced structure iteration process. Through this protocol, we take the pyrido[4,3-*d*]pyrimidine core group extracted from MRTX1133 [62] as the starting scaffold (details in Fig. 7 of SM), and we carry out three rounds of structural iterations to finally obtain a potential inhibitor template HM-387 for GTP-bound NRAS-R61 (as shown in Fig. 5 A). For the conceptual description of the method, see Section "Isomer-Sourced Structure Iteration" below and for the detailed

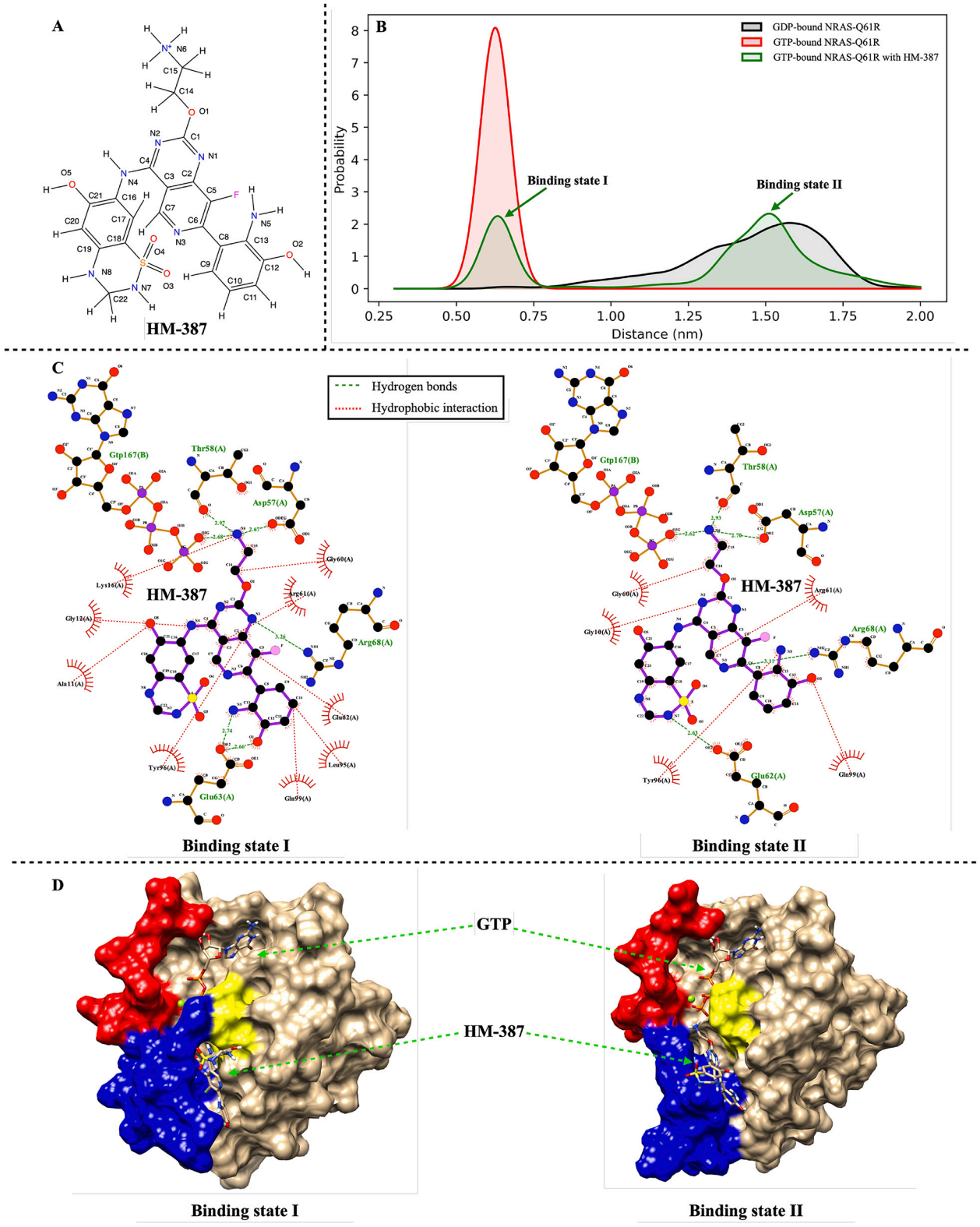

Fig. 5. HM-387 stably binds to the GTP-bound NRAS-R61 and can induce the behaviour of SW-II to the "off" state of GDP-bound NRAS-R61. (A) Structural diagram of HM-387, corresponding to the "Binding state I" (C); (B) Probability distribution of the distance between R61 and Pβ of GTP/GDP; (C) The binding state of HM-387 when bound to GTP-bound NRAS-R61; (D) Surface version of "Binding state I" and "Binding state II" (water molecules and ions are not shown).

iterative process, see Section "Full details of the drug design process" in SM.

In summary, considering the ligand/receptor flexibility as well as the distribution of charges and of surrounding water and ions, we proceed with a set of MD simulations (three independent trajectories of an HM-387+GTP-bound NRAS-R61, for a total 3 μs), that have been employed to explore in detail the dynamic binding model of HM-387 and the impact of HM-387 binding on GTP-bound NRAS-R61. The results of these MD simulations reveal in detail the active site of HM-387 and the interaction mode between HM-387 and GTP-bound NRAS-R61, as

shown in Fig. 5 C and D. From the analysis of trajectories, we have found that HM-387 has two binding states on the surface of GTP-bound NRAS-R61. First, HM-387 tightly binds to GTP-bound NRAS-R61 ("Binding state I"). As the simulation proceeds, HM-387 can induce the breakage of the HB between R61 and the GTP phosphate group and stabilise in a "Binding state II". Interestingly, the conformational characteristics of SW-II in "Binding state II" are very similar to the GDP-bound NRAS-R61 case. Moreover, the statistical results of the three independent trajectories show that the ratio of "Binding state I" and "Binding state II" is about 1:2. To demonstrate this more intuitively, we display the probability distribution of the distance between R61 and Pβ of GTP/GDP in Fig. 5 B. Overall, the combination of the three generations of structural iteration, docking analysis and MD simulation led to the design of HM-387, a potential selective inhibitor of NRAS-Q61 positively charged mutations.

3. Conclusions

The conformational characteristics of NRAS proteins and their underlying atom-level molecular interactions have been thoroughly analysed by means of extensive MD simulations and trajectory analysis. Q61 mutations can result in an altered modification of electric charge, which in turn alters the interaction of SW-II with its surroundings. The HB interactions of residue 61 with the Pγ phosphate group and residue 61 with water are crucial to the corresponding conformational changes of SW-II. With the occurrence of positively charged Q61 mutations (R61 and K61), the HB interactions between residue 61 and water are significantly enhanced. Due to the strong HB interaction between GTP phosphate group and R61/K61, SW-II maintains relatively low conformational fluctuations and there exists a small targetable pocket between α-helix 3. When GTP is converted to GDP, the HB interactions of residue 61 with water are enhanced as the interaction of residue 61 with the terminal phosphorus vanishes, causing SW-II to be separated from the protein surface and forming a huge cavity. In contrast, the L61 mutation reduces the affinity of SW-II to aqueous solution and the side chain of LEU can be captured by the hydrophobic pocket on the α-helix 3, thereby anchoring SW-II in the protein surface.

Given that the proportion of positively charged mutations in NRAS-Q61 is greater than 75%, then an isomer-sourced structure iteration method was proposed to design the potential inhibitors targeting the potentially druggable pocket of the NRAS positively charged mutation. In the Section "In silico development of potential inhibitors targeting NRAS-Q61 mutations using the ISSI method", considering GTP-bound NRAS-R61 only as an example, the whole process of designing and obtaining a prototype inhibitor (HM-387) by means of the ISSI method is fully demonstrated. The compound HM-387 can tightly bind to GTP-bound NRAS-R61 ("Binding state I") and gradually induce the protein conformation transition toward the "off-like" state ("Binding state II"). Switches between the two canonical states (active-inactive) of KRAS have been recently observed [63] by NMR measurements and related to the mechanism of action of a new covalent inhibitor (BBO-8956) of KRAS-G12C. This particular drug can significantly perturb the equilibrium of the on-off state and induce the GTP-bound KRAS-G12C species towards the inactive state. This also indicates the potential feasibility for targeting GTP-bound NRAS-Q61 positively charged mutations. In summary, the potential drug reported in the present work may be a first step towards the design of an effective inhibitor for NRAS-based cancers, although further development of the molecular design of the drug, based on wet-lab data, would be in order. We should point out that the synthesis and testing in a wet-lab of such a compound is a long and complex process and it has not been considered in the present work. In conclusion, we have disclosed the conformational changes of NRAS oncoproteins in detail at the atomic level and provided a new *in silico* drug design method called isomer-sourced structure iteration that can be useful for the discovery of potential inhibitors for oncogenes.

A final remark concerning potential extensions of this work: it would be of great interest a comparison of compounds obtained from ISSI with others designed using alternative techniques, or in the current case, the comparison of HM-387 to MRTX-1133 regarding the binding of such drugs to NRAS-R61. A way to carry out this comparison might be through the computation of Gibbs free-energy surfaces for the different drug bound at NRAS-GTP/GDP complexes. A series of metadynamics calculations of such free energies are currently underway in our lab.

4. Materials and methods

4.1. Setting of molecular dynamics simulation parameters

Our main computational tools have been microsecond scale MD, which is well suited to model a wide variety of biosystems at all-atom level, such as cell membranes [64,65], proteins [66] or micelles [67] to mention a few examples. In the present work we conducted MD simulations of eight NRAS isoforms with sequences represented in Fig. 1 of SM. Each system contained one isoform of the GTP or GDP bound NRAS complex fully solvated by 5,699 TIP3P water molecules [68] in potassium chloride solution (0.15 M) and magnesium chloride (0.03 M) yielding a system size of 19,900 atoms.

All MD inputs were generated by means of the CHARMM-GUI solution builder [69–71] assuming the CHARMM36m force field [31]. The different evolutions of his force field have been tested with high reliability throughout the last 20 years [72,31,73]. Our choice is due not only to its wide success in a large variety of biosystems, but because it includes the parameterisation of the species GTP and GDP (that can be found in the corresponding CHARMM36m topology file: https://www.charmm-gui.org/?doc=archive&lib=csml) and of many small-molecules. All bonds involving hydrogens were set to fixed lengths, allowing fluctuations of bond distances and angles for the remaining atoms. Crystal structures of GDP-bound NRAS and GTP-bound NRAS were downloaded from RCSB PDB Protein Data Bank [33], namely file names "6zio" and "5uhv". The sets of NRAS proteins (wild type, Q61R, Q61K and Q61L) were solvated in a water box, all systems were energy minimised and well equilibrated (NVT ensemble) before generating the production runs. 24 independent production runs were performed within the NPT ensemble for 9 μs (for a total 216 μs). All meaningful properties were averaged from 3 independent trajectories.

The pressure and temperature were set at 1 atm and 310.15 K respectively. In all MD simulations, the GROMACS/2021 package (version released on January 28th, 2021) was employed [32]. A time step of 2 fs was used in all equilibration and production simulations and the particle mesh Ewald method with Coulomb radius of 1.2 nm was employed to compute long-ranged electrostatic interactions. The cutoff for Lennard-Jones interactions was set to 1.2 nm. Pressure was controlled by a Parrinello-Rahman piston with damping coefficient of 5 ps^{-1} whereas temperature was controlled by a Nosé-Hoover thermostat with a damping coefficient of 1 ps^{-1}. Periodic boundary conditions in three directions of space have been taken. The MD simulation parameters for subsequent exploration of the binding mode of HM-387 and GTP-bound NRAS-Q61R are the same as above.

4.2. Trajectory analysis and visualisation

The GROMACS/2021 package [32] was employed for the MD simulations, whereas the software VMD [74], UCSF Chimera [75] and LigPlot$^+$ [76] for visualisation purposes and the R-package Bio3D [39] was used for trajectory analysis ("cross-correlation analysis").

4.3. Isomer-sourced structure iteration

In this section we provide an overview of the new protocol *isomer-sourced structure iteration*, including input content preparation, structure iteration and judging criteria. Compared with other virtual screening

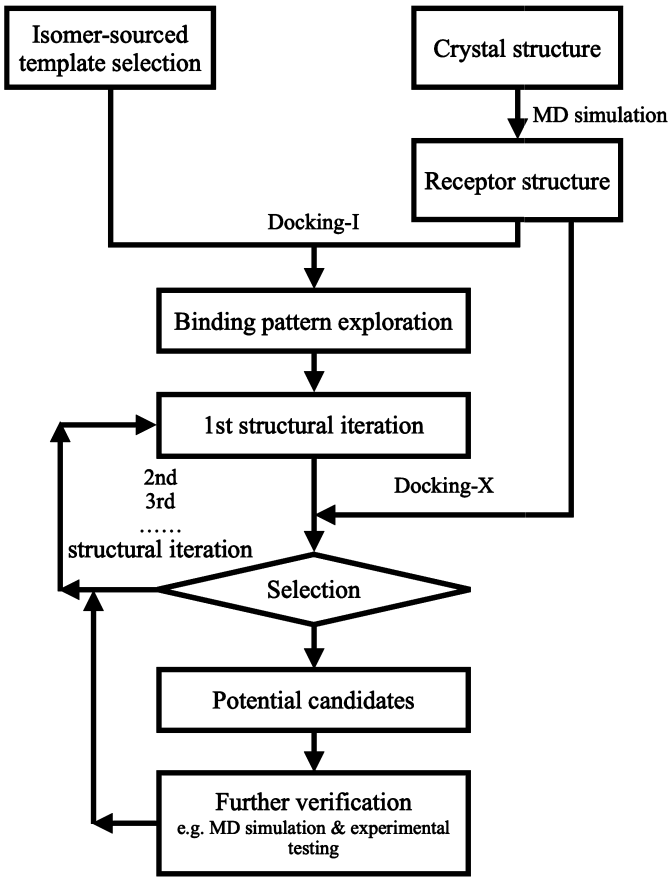

Fig. 6. Schematic diagram of the "Isomer-sourced structure iteration" *in silico* drug design method.

methods, the ISSI method has the following differences: (1) it uses the inhibitor's backbone structure of homologous proteins as starting templates, the structural similarity of homologous proteins may save the workload required for chemical structure template screening to a certain extent; (2) during the structure iteration, substituents are used as modular tools to splice with the template to quickly find the most suitable combination. In the current version reported here, the ISSI process follows the established procedure shown schematically in Fig. 6. It can be summarised as follows:

1. The input content mainly consists of "receptor structures" and a "isomer-sourced template". Here we used MD simulations to explore the impact of Q61 mutations on the NRAS conformational characteristics, and then obtain the "receptor structure" for the forthcoming structure iteration process.
2. The compound MRTX-1133 [62] was selected as the "isomer-sourced template" molecule, since MRTX-1133 can target the SW-II pocket of KRAS-G12D (between SW-II and α-helix 3 of KRAS-G12D). The action site of MRTX-1133 is close to the targetable pocket on the "receptor structure" (GTP-bound NRAS-Q61R). The binding pattern of "template" and "receptor" structures is studied through docking (here we named it "Docking-I"), and then the structural iteration sequence of the substituents is determined.
3. Subsequent structural iterations and the 3D models of the template molecule and subsequent iteration molecules were constructed by Cgen-FF [77,78]. We select the part of the template to stay unchanged (i.e. the "core"), whereas the remaining parts are considered as "substituent residues" (R_1, R_2, R_3). These residues can be any biological structure satisfying two conditions: (a) its docking score to the "receptor" is in a high (absolute) range and (b) it maximises the number of hydrogen-bonds that the residue can potentially form.
4. First structural iteration (core of MRTX-1133 + substituent R_1, keeping R_2 and R_2 unchanged). Then the structure generated by structure iteration is docked (Docking-X) with the receptor, to select the optimal R_1. Second structural iteration, fixing the selected R_1 and the original R_3, then iterating R_2. Third structural iteration, fixing the selected R_1 and R_2, then iterating R_3.
5. The potential candidates formed by the "core" and three selected residues will be further verified by further MD simulations or experimental test (if conditions permit it). The reader should notice that the number of structural iterations can be increased or decreased as needed. In the present work, as a sort of a benchmark example, we set up three generations of structural iterations for R_1, R_2, R_3 and finally we get the potential candidate HM-387 (process shown in Fig. 8 of SM and the final prototype shown in Fig. 5).

CRediT authorship contribution statement

Zheyao Hu: Writing – review & editing, Writing – original draft, Visualization, Validation, Software, Methodology, Investigation, Formal analysis, Data curation, Conceptualization. **Jordi Martí:** Writing – review & editing, Writing – original draft, Validation, Supervision, Project administration, Methodology, Investigation, Funding acquisition, Formal analysis, Data curation, Conceptualization.

Declaration of competing interest

The authors declare that they have no known competing financial interests or personal relationships that could have appeared to influence the work reported in this paper.

Data and software availability

The crystal structure files, MD simulation files (input files, parameter files, topology files etc.), structures of small molecule mentioned in the ISSI drug design process, all the above documents are available on the website (https://github.com/Zheyao-Hu/NRAS-Research). Moreover, all software (free to use) mentioned in the text is the official release version without any modification.

Acknowledgements

This publication is funded by the project with grant number MCIN/AEI/PID2021-124297NB-C32, awarded by the Spanish Ministry of Science, Innovation and Universities MCIN/AEI/10.13-039/5011000-11033 and "FEDER Una manera de hacer Europa". Zheyao Hu is a Ph.D. fellow from the China Scholarship Council (grant 202006230070). J.M. thanks the *Generalitat de Catalunya* for the support through the grant *Grup de Recerca SGR-Cat2021 Condensed, Complex and Quantum Matter Group* reference 2021SGR-01411 and to the Polytechnic University of Catalonia-Barcelona Tech through the funding AGRUPS. Finally, computational resources provided by the Barcelona Supercomputing Center, project BCV-2023-2-0004 are also acknowledged.

Appendix A. Supplementary material

Supplementary material related to this article can be found online at https://doi.org/10.1016/j.csbj.2024.05.038.

References

[1] Li S, Balmain A, Counter CM. A model for ras mutation patterns in cancers: finding the sweet spot. Nat Rev Cancer 2018;18(12):767–77.
[2] Moore AR, Rosenberg SC, McCormick F, Malek S. Ras-targeted therapies: is the undruggable drugged? Nat Rev Drug Discov 2020;19(8):533–52.

[3] Prior IA, Hood FE, Hartley JL. The frequency of ras mutations in cancer. Cancer Res 2020;80(14):2969–74.
[4] Nagarajan P, Asgari MM, Green AC, Guhan SM, Arron ST, Proby CM, et al. Keratinocyte carcinomas: current concepts and future research priorities. Clin Cancer Res 2019;25(8):2379–91.
[5] Schadendorf D, van Akkooi AC, Berking C, Griewank KG, Gutzmer R, Hauschild A, et al. Lancet 2018;392(10151):971–84.
[6] Johnson DB, Puzanov I. Treatment of nras-mutant melanoma. Curr Treat Options Oncol 2015;16:1–12.
[7] Randic T, Kozar I, Margue C, Utikal J, Kreis S. Nras mutant melanoma: towards better therapies. Cancer Treat Rev 2021;99:102238.
[8] Fedorenko IV, Gibney GT, Smalley KS. Nras mutant melanoma: biological behavior and future strategies for therapeutic management. Oncogene 2013;32(25):3009–18.
[9] Johnson DB, Lovly CM, Flavin M, Panageas KS, Ayers GD, Zhao Z, et al. Impact of nras mutations for patients with advanced melanoma treated with immune therapies. Cancer Immunol Res 2015;3(3):288–95.
[10] Davis LE, Shalin SC, Tackett AJ. Current state of melanoma diagnosis and treatment. Cancer Biol Ther 2019;20(11):1366–79.
[11] Gureghian V, Herbst H, Kozar I, Mihajlovic K, Malod-Dognin N, Ceddia G, et al. A multi-omics integrative approach unravels novel genes and pathways associated with senescence escape after targeted therapy in nras mutant melanoma. Cancer Gene Ther 2023:1–16.
[12] Fda authorized drugs for melanoma. Available from: https://www.fda.gov/drugs/resources-information-approved-drugs/fda-approves-encorafenib-and-binimetinib-combination-unresectable-or-metastatic-melanoma-braf, 2018.
[13] DiMasi JA, Grabowski HG, Hansen RW. Innovation in the pharmaceutical industry: new estimates of r&d costs. J Health Econ 2016;47:20–33.
[14] Chang Y, Hawkins BA, Du JJ, Groundwater PW, Hibbs DE, Lai F. A guide to in silico drug design. Pharmaceutics 2023;15(1):49.
[15] Karplus M, Petsko GA. Molecular dynamics simulations in biology. Nature 1990;347:631–9.
[16] Karplus M, McCammon JA. Molecular dynamics simulations of biomolecules. Nat Struct Biol 2002;9(9):646–52.
[17] Rapaport DC, Rapaport DCR. The art of molecular dynamics simulation. Cambridge University Press; 2004.
[18] Shoichet BK. Virtual screening of chemical libraries. Nature 2004;432(7019):862–5.
[19] Alonso H, Bliznyuk AA, Gready JE. Combining docking and molecular dynamic simulations in drug design. Med Res Rev 2006;26(5):531–68.
[20] Damm KL, Carlson HA. Exploring experimental sources of multiple protein conformations in structure-based drug design. J Am Chem Soc 2007;129(26):8225–35.
[21] Schmidt T, Bergner A, Schwede T. Modelling three-dimensional protein structures for applications in drug design. Drug Discov Today 2014;19(7):890–7.
[22] Gupta R, Srivastava D, Sahu M, Tiwari S, Ambasta RK, Kumar P. Artificial intelligence to deep learning: machine intelligence approach for drug discovery. Mol Divers 2021;25:1315–60.
[23] Gorgulla C, Boeszoermenyi A, Wang Z-F, Fischer PD, Coote PW, Padmanabha Das KM, et al. An open-source drug discovery platform enables ultra-large virtual screens. Nature 2020;580(7805):663–8.
[24] Brogi S, Ramalho TC, Kuca K, Medina-Franco JL, Valko M. In silico methods for drug design and discovery. Front Chem 2020;8:612.
[25] Cai C, Wang S, Xu Y, Zhang W, Tang K, Ouyang Q, et al. Transfer learning for drug discovery. J Med Chem 2020;63(16):8683–94.
[26] Li Y, Pei J, Lai L. Structure-based de novo drug design using 3d deep generative models. Chem Sci 2021;12(41):13664–75.
[27] Guo Q, Zhang H, Deng Y, Zhai S, Jiang Z, Zhu D, et al. Ligand-and structural-based discovery of potential small molecules that target the colchicine site of tubulin for cancer treatment. Eur J Med Chem 2020;196:112328.
[28] Sadybekov AA, Sadybekov AV, Liu Y, Iliopoulos-Tsoutsouvas C, Huang X-P, Pickett J, et al. Synthon-based ligand discovery in virtual libraries of over 11 billion compounds. Nature 2022;601(7893):452–9.
[29] Xu L, Zhang Y, Zheng L, Qiao C, Li Y, Li D, et al. Discovery of novel inhibitors targeting the macrophage migration inhibitory factor via structure-based virtual screening and bioassays. J Med Chem 2014;57(9):3737–45.
[30] Frenkel D, Smit B. Understanding molecular simulation: from algorithms to applications. San Diego: Academic Press; 2002.
[31] Huang J, MacKerell Jr AD. Charmm36 all-atom additive protein force field: validation based on comparison to nmr data. J Comput Chem 2013;34(25):2135–45.
[32] Berendsen HJ, van der Spoel D, van Drunen R. Gromacs: a message-passing parallel molecular dynamics implementation. Comput Phys Commun 1995;91(1–3):43–56.
[33] Kouranov A, Xie L, de la Cruz J, Chen L, Westbrook J, Bourne PE, et al. The rcsb pdb information portal for structural genomics. Nucleic Acids Res 2006;34(suppl_1):D302–5.
[34] Hu Z, Marti J. Discovering and targeting dynamic drugging pockets of oncogenic proteins: the role of magnesium in conformational changes of the g12d mutated kirsten rat sarcoma-guanosine diphosphate complex. Int J Mol Sci 2022;23(22):13865.
[35] Nussinov R, Tsai C-J, Jang H. Oncogenic ras isoforms signaling specificity at the membrane. Cancer Res 2018;78(3):593–602.
[36] Moore AR, Rosenberg SC, McCormick F, Malek S. Ras-targeted therapies. Nat Rev Drug Discov 2021.
[37] Lu H, Martí J. Predicting the conformational variability of oncogenic gtp-bound g12d mutated kras-4b proteins at zwitterionic model cell membranes. Nanoscale 2022;14(8):3148–58.
[38] Ichiye T, Karplus M. Collective motions in proteins: a covariance analysis of atomic fluctuations in molecular dynamics and normal mode simulations. Proteins, Struct Funct Bioinform 1991;11(3):205–17.
[39] Grant BJ, Rodrigues AP, ElSawy KM, McCammon JA, Caves LS. Bio3d: an r package for the comparative analysis of protein structures. Bioinformatics 2006;22(21):2695–6.
[40] Lu S, Jang H, Muratcioglu S, Gursoy A, Keskin O, Nussinov R, et al. Ras conformational ensembles, allostery, and signaling. Chem Rev 2016;116(11):6607–65.
[41] Hobbs GA, Der CJ, Rossman KL. Ras isoforms and mutations in cancer at a glance. J Cell Sci 2016;129(7):1287–92.
[42] Omholt K, Karsberg S, Platz A, Kanter L, Ringborg U, Hansson J. Screening of n-ras codon 61 mutations in paired primary and metastatic cutaneous melanomas: mutations occur early and persist throughout tumor progression. Clin Cancer Res 2002;8(11):3468–74.
[43] Burd CE, Liu W, Huynh MV, Waqas MA, Gillahan JE, Clark KS, et al. Mutation-specific ras oncogenicity explains nras codon 61 selection in melanoma. Cancer Discov 2014;4(12):1418–29.
[44] Hu Z, Martí J, Lu H. Structure of benzothiadiazine at zwitterionic phospholipid cell membranes. J Chem Phys 2021;155(15):154303.
[45] Hu Z, Marti J. In silico drug design of benzothiadiazine derivatives interacting with phospholipid cell membranes. Membranes 2022;12(3):331.
[46] Chandler D. Introduction to modern statistical mechanics. Oxford University Press; 1987.
[47] Lu H, Marti J. Binding free energies of small-molecules in phospholipid membranes: aminoacids, serotonin and melatonin. Chem Phys Lett 2018;712:190–5.
[48] Bussi G, Gervasio FL, Laio A, Parrinello M. Free-energy landscape for β hairpin folding from combined parallel tempering and metadynamics. J Am Chem Soc 2006;128(41):13435–41.
[49] Barducci A, Bonomi M, Parrinello M. Metadynamics. Wiley Interdiscip Rev Comput Mol Sci 2011;1(5):826–43.
[50] Martí J, Csajka FS, Chandler D. Stochastic transition pathways in the aqueous sodium chloride dissociation process. Chem Phys Lett 2000;328(1):169–76.
[51] Martí J, Csajka FS. Transition path sampling study of flip-flop transitions in model lipid bilayer membranes. Phys Rev E 2004;69(6):061918.
[52] Dellago C, Bolhuis PG. Transition path sampling simulations of biological systems. In: Atomistic approaches in modern biology. Springer; 2006. p. 291–317.
[53] Frech M, Darden T, Pedersen L, Foley C, Charifson P, Anderson M, et al. Role of glutamine-61 in the hydrolysis of gtp by p21h-ras: an experimental and theoretical study. Biochemistry 1994;33(11):3237–44.
[54] Tichauer RH, Favre G, Cabantous S, Landa G, Hemeryck A, Brut M. Water distribution within wild-type nras protein and q61 mutants during unrestrained qm/mm dynamics. Biophys J 2018;115(8):1417–30.
[55] Novelli ET, First JT, Webb LJ. Quantitative measurement of intrinsic gtp hydrolysis for carcinogenic glutamine 61 mutants in h-ras. Biochemistry 2018;57(44):6356–66.
[56] Tichauer RH, Favre G, Cabantous S, Brut M. Hybrid qm/mm vs pure mm molecular dynamics for evaluating water distribution within p21n-ras and the resulting gtp electronic density. J Phys Chem B 2019;123(18):3935–44.
[57] Maegley KA, Admiraal SJ, Herschlag D. Ras-catalyzed hydrolysis of gtp: a new perspective from model studies. Proc Natl Acad Sci 1996;93(16):8160–6.
[58] McGrath JP, Capon DJ, Goeddel DV, Levinson AD. Comparative biochemical properties of normal and activated human ras p21 protein. Nature 1984;310(5979):644–9.
[59] Sweet RW, Yokoyama S, Kamata T, Feramisco JR, Rosenberg M, Gross M. The product of ras is a gtpase and the t24 oncogenic mutant is deficient in this activity. Nature 1984;311(5983):273–5.
[60] Trahey M, McCormick F. A cytoplasmic protein stimulates normal n-ras p21 gtpase, but does not affect oncogenic mutants. Science 1987;238(4826):542–5.
[61] Adari H, Lowy DR, Willumsen BM, Der CJ, McCormick F. Guanosine triphosphatase activating protein (gap) interacts with the p21 ras effector binding domain. Science 1988;240(4851):518–21.
[62] Wang X, Allen S, Blake JF, Bowcut V, Briere DM, Calinisan A, et al. Identification of mrtx1133, a noncovalent, potent, and selective krasg12d inhibitor. J Med Chem 2021;65(4):3123–33.
[63] Sharma AK, Pei J, Yang Y, Dyba M, Smith B, Rabara D, et al. Revealing the mechanism of action of a first-in-class covalent inhibitor of krasg12c (on) and other functional properties of oncogenic kras by 31p nmr. J Biol Chem 2024;300(2):105650.
[64] Yang J, Martí J, Calero C. Pair interactions among ternary dppc/popc/cholesterol mixtures in liquid-ordered and liquid-disordered phases. Soft Matter 2016;12(20):4557–61.
[65] Lu H, Marti J. Cellular absorption of small molecules: free energy landscapes of melatonin binding at phospholipid membranes. Sci Rep 2020;10(1):9235.
[66] Henry ER, Best RB, Eaton WA. Comparing a simple theoretical model for protein folding with all-atom molecular dynamics simulations. Proc Natl Acad Sci 2013;110(44):17880–5.
[67] Rodriguez J, Martí J, Guardia E, Laria D. Protons in non-ionic aqueous reverse micelles. J Phys Chem B 2007;111(17):4432–9.
[68] Jorgensen WL, Chandrasekhar J, Madura JD, Impey RW, Klein ML. Comparison of simple potential functions for simulating liquid water. J Chem Phys 1983;79(2):926–35.

[69] Jo S, Kim T, Iyer VG, Im W. Charmm-gui: a web-based graphical user interface for charmm. J Comput Chem 2008;29(11):1859–65.
[70] Brooks BR, Brooks III CL, Mackerell Jr AD, Nilsson L, Petrella RJ, Roux B, et al. Charmm: the biomolecular simulation program. J Comput Chem 2009;30(10):1545–614.
[71] Lee J, Cheng X, Swails JM, Yeom MS, Eastman PK, Lemkul JA, et al. Charmm-gui input generator for namd, gromacs, amber, openmm, and charmm/openmm simulations using the charmm36 additive force field. J Chem Theory Comput 2016;12(1):405–13.
[72] Vanommeslaeghe K, Hatcher E, Acharya C, Kundu S, Zhong S, Shim J, et al. Charmm general force field: a force field for drug-like molecules compatible with the charmm all-atom additive biological force fields. J Comput Chem 2010;31(4):671–90.
[73] Huang J, Rauscher S, Nawrocki G, Ran T, Feig M, De Groot BL, et al. Charmm36m: an improved force field for folded and intrinsically disordered proteins. Nat Methods 2017;14(1):71–3.
[74] Humphrey W, Dalke A, Schulten K. Vmd: visual molecular dynamics. J Mol Graph 1996;14(1):33–8.
[75] Pettersen EF, Goddard TD, Huang CC, Couch GS, Greenblatt DM, Meng EC, et al. Ucsf chimera—a visualization system for exploratory research and analysis. J Comput Chem 2004;25(13):1605–12.
[76] Laskowski RA, Swindells MB. Ligplot+: multiple ligand–protein interaction diagrams for drug discovery; 2011.
[77] Vanommeslaeghe K, MacKerell Jr AD. Automation of the charmm general force field (cgenff) i: bond perception and atom typing. J Chem Inf Model 2012;52(12):3144–54.
[78] Vanommeslaeghe K, Raman EP, MacKerell Jr AD. Automation of the charmm general force field (cgenff) ii: assignment of bonded parameters and partial atomic charges. J Chem Inf Model 2012;52(12):3155–68.